

THE GAS-GALAXY CONNECTION AT $z_{\text{abs}} = 0.35$: O VI AND H I ABSORPTION TOWARDS J0943+0531

C. THOM^{1,2}, J. K. WERK³, J. TUMLINSON², J. X. PROCHASKA³, J. D. MEIRING⁴, T. M. TRIPP⁴, K. R. SEMBACH²

Draft version April 26, 2021

ABSTRACT

We present observations of H I and O VI absorption systems proximate to a galaxy at $z_{\text{gal}} = 0.3529$. The absorption was detected serendipitously in *Cosmic Origins Spectrograph* observations of the low- z QSO J0943+0531 ($z_{\text{QSO}} = 0.564$). The data show two separate clouds along the sightline at an impact parameter of 95 kpc from the galaxy. The first is likely low-metallicity gas falling onto the galaxy. This assessment is based on the high velocity offset of the cloud from the galaxy ($\Delta v = 365 \text{ km s}^{-1}$) and the weak metal line absorption, combined with photoionization modeling. The second cloud, with only a modest velocity separation from the galaxy ($\Delta v = 85 \text{ km s}^{-1}$), exhibits very strong O VI absorption qualitatively similar to O VI absorption seen in the Milky Way halo. Collisional ionization equilibrium models are ruled out by the metal line column density ratios. Photoionization modeling implies a length-scale for the O VI cloud of $\sim 0.1\text{--}1.2 \text{ Mpc}$, which indicates the absorbing gas most likely resides within the local filamentary structure. This system emphasizes that kinematic association alone is not sufficient to establish a physical connection to galaxies, even at small impact parameters and velocity separations. Observations such as these, connecting galaxies with their gaseous environments, are becoming increasingly important for understanding of galaxy evolution and provide constraints for cosmological simulations.

Subject headings: galaxies: halos—intergalactic medium—quasars: absorption lines

1. INTRODUCTION

Two of the most important unanswered questions in galaxy formation concern how galaxies acquire their gas, and how they recycle it back into their circumgalactic medium (CGM) and the intergalactic medium (IGM). The starlight of galaxies is relatively easy to observe, and recent surveys such as the Sloan Digital Sky Survey (SDSS; York et al. 2000) have yielded uniformly selected, statistical characterizations of galaxies, such as the luminosity function (Blanton et al. 2003), the mass-metallicity relation (Tremonti et al. 2004) and color-magnitude diagram (Strateva et al. 2001; Kauffmann et al. 2003).

By contrast with the stars, the gaseous environments of galaxy halos are poorly understood. H I 21 cm observations are only possible for the closest galaxies, while QSO absorption line studies have been plagued by small sample sizes, and the ambiguity of associating absorption systems with the nearby galaxy population. To investigate this crucial aspect of galaxy evolution we have embarked on a program to empirically characterize gas in the halos of galaxies. Our Cycle 17 Hubble Space Telescope (HST) large program (PI Tumlinson; PID 11598) will obtain spectra of 39 QSOs, which were selected to lie behind $L \geq L^*$ “target” galaxies at $z = 0.1\text{--}0.3$, while our Cycle 18 HST program (PI Tumlinson; PID 12204) will improve coverage of the galaxy luminosity function by observing 41 sightlines that pass through dwarf galaxy halos. The goal of the survey is to systematically map the

multiphase gaseous structure of galaxy halos on 100 kpc scales, with the aim of unraveling their feedback and accretion processes.

In the Milky Way, gas has been observed in the halo since the early 1960s, both in the 21 cm emission of neutral hydrogen (Muller et al. 1963; Barnes et al. 2001; Kalberla et al. 2005), as well as UV and optical absorption lines (e.g. Münch & Zirin 1961; van Woerden et al. 1999; Tripp et al. 2003; Sembach et al. 2003; Richter et al. 2005; Thom et al. 2006, 2008; Ben Bekhti et al. 2008; Collins et al. 2009). In order to differentiate halo clouds from disk material, selection is typically based on the radial velocity of the cloud. Halo clouds with high velocities relative to the Local Standard of Rest ($v_{\text{LSR}} > 100 \text{ km s}^{-1}$) are thus deemed high-velocity clouds (HVCs; Wakker & van Woerden 1997). Due to this velocity selection, we may be missing some of the halo clouds when studying the MW as low-velocity halo clouds are hard to distinguish from the disk (Peek et al. 2009).

The 21 cm HVCs trace only the highest column density systems ($N_{\text{H I}} \gtrsim 10^{18} \text{ cm}^{-2}$; Putman et al. 2003b; Kalberla et al. 2005) and they represent flow of gas into and out of the disk of the Galaxy. They may provide fresh fuel for star-formation in the disk, either accreted directly from the IGM, or stripped from dwarf satellite galaxies. Alternatively, they may be part of outflowing galactic waste, expelled from the disk by supernova driven winds. Many of these high column density systems lie within $\sim 10\text{--}20 \text{ kpc}$ (van Woerden et al. 1999; Thom et al. 2006; Wakker et al. 2007; Thom et al. 2008; Lehner & Howk 2010; Tripp & Song 2011), as determined by foreground/background stellar probes at known distances. The exception—the Magellanic Stream—is typically assumed to be at the same distance as the Magellanic Clouds ($\sim 50 \text{ kpc}$).

¹ cthom@stsci.edu

² Space Telescope Science Institute, 3700 San Martin Dr, Baltimore MD, 21211, U.S.A

³ UCO/Lick Observatory, University of California, 1156 High Street, Santa Cruz, CA 95064, USA

⁴ Department of Astronomy, University of Massachusetts, 710 North Pleasant Street, Amherst, MA 01003, USA

Under the current paradigm, the volume between the the cool, dense halo clouds is filled with a tenuous, low-density, hot halo corona. Its existence was first proposed by Spitzer (1956) as the medium which held the observed cool clouds in pressure equilibrium, and it is a universal prediction of numerical simulations of L^* galaxies (e.g. White & Rees 1978; Kereš et al. 2009). For a Milky Way sized halo, accreting gas is expected to be shock-heated to the virial temperature of $\sim 10^6$ K (Birnbom & Dekel 2003). Galactic outflows may also contribute a substantial amount of hot material (Oppenheimer & Davé 2009).

This hot, low-density gas is difficult to detect directly. Its effect is seen indirectly as a drag force on clouds moving through it (Peek et al. 2007), which results in a pronounced head-tail structure as the denser cool clouds are slowly ablated. This is an effect seen both in simulations (Quilis & Moore 2001; Heitsch & Putman 2009) and radio observations (Westmeier et al. 2005). X-ray absorption towards the LMC X-3 X-ray source provides evidence that the halo gas is hot (Wang et al. 2005). A sample of 25 O VII $K\alpha$ detections also favors an explanation in MW hot halo gas (as opposed to a Local Group origin; Bregman & Lloyd-Davies 2007, and references therein)

Further evidence for this hot halo corona comes from the O VI absorption line in the UV (Sembach et al. 2003, hereafter S03). O VI traces gas at $\log T \sim 5.5$ in collision ionization equilibrium (Sutherland & Dopita 1993). Using an extensive survey of 102 AGN sightlines passing through the halo, S03 found a covering fraction of 65 – 85% for column densities in the range $\log N_{\text{O VI}} = 13 - 14.5$. Some of the Milky Way O VI is associated with the H I HVCs and likely arises in interface layers between cool and hot gas. Some detections, however, were not correlated with detectable H I absorption or emission, and favor an extended ($R \gtrsim 70$ kpc), hot ($T > 10^6$ K) halo. This conclusion was based on the column density ratios of O VI to other highly ionized species (such as N V and C IV), as well as a strong correlation between $N_{\text{O VI}}$ and the line widths (S03).

In QSO sightlines probing the IGM and low- z galaxy halos, the physical conditions of O VI absorbers are harder to determine, as it is harder to distinguish between collisional ionization in hot gas, and cool gas photoionized by the meta-galactic UV background field. O VI can be found in a diverse range of environments, from galaxies to groups, filaments and the IGM (Savage et al. 1998; Tripp & Savage 2000; Tripp et al. 2001; Prochaska et al. 2006; Stocke et al. 2006; Lehner et al. 2009; Prochaska et al. 2011). Several studies have shown a correlation with galaxies on large spatial scales (e.g. Stocke et al. 2006; Prochaska et al. 2011), and there appears to be a correlation with emission-line dominated galaxies (Chen & Mulchaey 2009). Several recent statistical surveys have studied O VI in the low- z IGM with the Space Telescope Imaging Spectrograph (STIS) (Tripp et al. 2008; Danforth & Shull 2008; Thom & Chen 2008a), but while some of the gas can be shown to be cool (Tripp et al. 2006; Thom & Chen 2008b), much of it is multi-phase gas or its ionization state cannot be determined (e.g. Tripp et al. 2008; Thom & Chen 2008b). O VI is thus a useful gas diagnostic, but is sometimes am-

Table 1
Summary of the COS Observations

Dataset	Grating	Cenwave (Å)	Coverage (Å)	t_{exp} (s)
lb5n42qgq	G130M	1291	1132 – 1433	2101
lb5n42qlq	G130M	1309	1153 – 1440	1561
lb5n42qqq	G160M	1600	1410 – 1772	1177
lb5n42qsq	G160M	1600	1410 – 1772	804
lb5n42qvq	G160M	1623	1433 – 1796	1964

Note. — Journal of COS Observations of SDSS J094331.61+053131.4 at $z_{\text{QSO}} = 0.564$.

biguous, and does not correspond to a unique environment. The installation of the Cosmic Origins Spectrograph (COS; Green et al. 2003) on-board HST has dramatically opened up the number of QSOs available for detailed studies of O VI in the low- z IGM and galaxy halos, and several recent results have reported analyses of individual low- z O VI systems (Savage et al. 2010; Danforth et al. 2010; Savage et al. 2011; Yao et al. 2011).

Here we report the serendipitous detection of halo O VI absorption and metal-poor gas in or near a galaxy halo at $z = 0.35$. This galaxy was not the targeted galaxy, and thus the detections are truly serendipitous; initial statistical analysis of all the survey targets will be presented in a forthcoming series of publications (Tumlinson et al., in prep). The absorbers are detected at an impact parameter of $\rho = 95$ kpc. The O VI cloud may be tracing a photoionized filamentary structure near the galaxy, while the metal-poor cloud is more likely to be tracing gas infall into the galaxy halo. Companion papers by Tumlinson et al. (2011) and Meiring et al. (2011) present other first results from our Cycle 17 halos survey, including the observation of the strongest O VI absorber seen in the low- z IGM, and initial results on the first sample of damped Ly α absorbers detected with COS (respectively). In Section 2 we describe the observations and data reduction. Section 3 gives the main results, and Section 4 discusses the implications for the Milky Way and galaxies in general. When necessary, we adopt a flat cosmology with $\Omega_m = 0.27$, $\Omega_\Lambda = 0.73$ and $H_0 = 71 \text{ km s}^{-1} \text{ Mpc}^{-1}$.

2. DATA

2.1. COS Spectroscopy

The UV spectrum of the quasar SDSS J094331.61+053131.4 (hereafter J0943+0531) was obtained with COS on 06 March 2010. The raw data were processed through the standard COS reduction and calibration pipeline, *calcos* (v2.12). More detailed information can be found in the COS instrument handbook⁵. We obtained spectra with both medium resolution FUV gratings, G130M and G160M. Table 1 shows a journal of the observations, grating settings, and exposure times.

We developed software to align and co-add the individual, calibrated x1d spectra output by *calcos*. Since much of our data is in the low count regime ($N < 30$), we operated directly on photon counts, rather than flux calibrated data. This allowed us to correctly estimate the Poisson errors associated with the number of counts in a given pixel (Gehrels 1986). Each exposure with a given

⁵ <http://www.stsci.edu/hst/cos/documents/handbooks/>

grating and central wavelength setting was co-aligned using common Galactic absorption lines to determine the relative shifts between the individual exposures. The exposures were then shifted to a common reference and co-added. This process was performed individually for each detector segment. The two detector segments for each grating were then aligned with each other using absorption lines of similar strengths (e.g. Si III 1206 vs C II 1334). Finally, the G130M and G160M spectra were co-aligned and co-added using lines of the same species (e.g. Si II 1260 vs Si II 1526).

Co-addition was performed by a simple sum of counts, after alignment. For each pixel, we tracked the wavelength, number of counts, upper and lower error estimates due to Poisson statistics, and the effective exposure time. We applied a flat-field correction by taking the STScI COS team 1d flats (D. Massa, priv. comm.), processed with a low-pass filter, to remove the high-frequency noise. These flats account for the grid-wire pattern in the COS FUV detectors, and are applied to the effective exposure time for each pixel (note that they are not applied to the counts directly, since we use the counts to calculate the Poisson errors). Since we accumulate counts, the spectra contain sharp discontinuities in regions where the wavelength dithering resulted in a larger effective exposure time, or in regions affected by the grid-wire pattern. Thus our counts spectra do not have a smooth continuum but the count *rate* spectrum does.

Finally, we normalized the count-rate spectrum by piecewise fitting of low-order Chebyshev polynomials to chunks of spectrum $\sim 50 - 100 \text{ \AA}$ long. Our procedure yields a normalized spectrum with both upper and lower error estimates. In regions of high counts ($\gtrsim 30$), these estimates converge to the usual gaussian approximation of \sqrt{N} , with the upper and lower estimates the same (i.e. converging to the usual 1σ errors). To be conservative, when quoting errors on measured quantities, we quote the larger of these two error estimates.

The S/N of the resulting spectra varies from ~ 4 per resolution element⁶ at the shortest wavelengths ($\sim 1135 \text{ \AA}$), peaking at ~ 8 per resel at $\sim 1400 \text{ \AA}$, and declining to $\sim 2 - 3$ per resel at the red end of the spectrum ($\sim 1800 \text{ \AA}$). By choosing multiple appropriate central wavelength settings for each grating, we ensured continuous wavelength coverage (i.e. no gaps), at the expense of lower S/N in the wavelength regions with only one grating setting.

2.2. Keck HIRES Spectroscopy

We obtained a high resolution optical spectrum of J0943+0531 on 26 March 2010 using the High Resolution Echelle Spectrometer (HIRES; Vogt et al. 1994) on Keck I. We employed the UV cross-disperser and the C1 decker (slit width $0.86''$), resulting in a resolution of ~ 48000 or $\sim 6 \text{ km s}^{-1}$. The grating angles were set to give coverage down to 3050 \AA , in order to detect low- z

Mg II absorption. The data were reduced with the HIREDUX pipeline included with the XIDL package⁷. Individual orders were normalized after extraction with a series of Chebyshev polynomials to remove the echelle blaze function, and then combined into a final 1D spectrum.

2.3. Galaxy Spectroscopy

After the COS observations were conducted we obtained spectra of several galaxies in the field close to the QSO with the Low Resolution Imaging Spectrometer (LRIS; Oke et al. 1995) on the Keck I telescope. We obtained long-slit spectra of 4 galaxies on 25 March 2010. We employed the 5600 \AA dichroic, with the $600/7500$ grating on the red side, and the $600/4000$ grism on the blue side. The slit size was $1''$, yielding a FWHM resolution of 4.7 \AA ($\sim 200 \text{ km s}^{-1}$) over a wavelength range of $5600 - 8200 \text{ \AA}$ on the red side; the blue side covered the range $3000 - 5500 \text{ \AA}$ at a resolution of $3.9 - 4.1 \text{ \AA}$ FWHM ($\sim 300 \text{ km s}^{-1}$). The data were reduced using the LRIS pipeline in the XIDL package.

Fig 1 shows an image of the field taken from the SDSS, centered on the QSO position. Objects classified as galaxies in SDSS are labeled in a polar co-ordinate system, with a position angle (degrees east of north) and an angular distance from the QSO (in arcsec). Galaxies for which we obtained spectroscopic redshifts are enclosed in red boxes, and the measured redshifts included in the label. Objects classified as galaxies in SDSS but which lack spectroscopic redshifts are enclosed in green diamonds. The maximum range of the SDSS photometric redshift estimates are listed. We have also examined the photometric redshift probability distributions for these objects produced by Cunha et al. (2009). None of these objects are consistent with being at the redshift of the absorbers, although we note that contamination of objects very close to the QSO by the QSO light may be an issue, and it would be ideal to obtain further spectroscopy follow-up for these galaxies. Unlabeled objects in Figure 1 are classified as stars. Higher resolution imaging with e.g. HST, is an ongoing component of our multi-instrument project, and would be helpful in the future for quantitative measures of galaxy morphology.

3. RESULTS

3.1. Absorption Lines

In Figure 2 we show the absorption lines affiliated with the galaxy 227_19. We plot the continuum normalized spectra in a velocity space, with respect to the spectroscopic redshift of the galaxy, $z_{\text{gal}} = 0.3529$ (all velocities in this paper are with respect to this zero-point).

At $v = +365 \text{ km s}^{-1}$ we detect strong saturated Ly α absorption. The first 5 H I lines are saturated, and the system breaks into two main components in the higher order Lyman lines, at velocities of $v = +365, +445 \text{ km s}^{-1}$. Both components have associated weak C III absorption. The spectrum also shows a hint of possible O VI absorption, but these features are only significant at the 2σ level, and we consider them non-detections. Higher quality data would be required to confirm these features. Significantly, we detect no Mg II

⁶ The COS detector and calcos oversamples the resolution element with 6 detector ‘‘pixels’’, which are defined by the clock resolution and electronics of the detector. We bin the resulting spectra by 3 pixels. This retains Nyquist sampling of the resolution element, but improves the S/N.

⁷ <http://www.ucolick.org/~xavier/HIREdux/index.html>

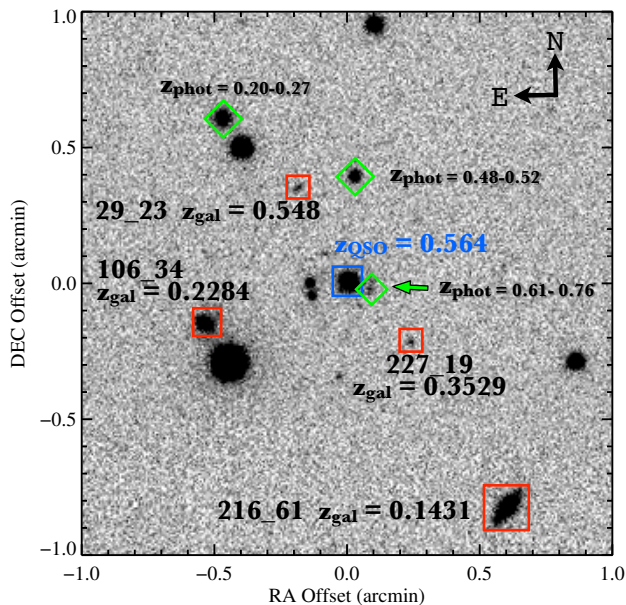


Figure 1. SDSS i -band image of the field around J0943+0531. The QSO is centered and surrounded with a blue box. Galaxies are labeled with a polar co-ordinate system based on the position angle (degrees east of north) and the angular separation from the QSO (arcsec). Galaxies with spectroscopic redshifts are enclosed in red boxes, while galaxies with only photometric estimates are enclosed in green diamonds. Objects not labeled are stars.

absorption in the HIRES data to very sensitive upper limits. Due to its lack of strong metal line absorption, we describe this cloud as “metal-poor”, a name we will justify in Section 4.1. This system also contains a much weaker H I component at $+285 \text{ km s}^{-1}$ with no associated metal absorption. Figure 2 shows the first 3 Lyman series lines, as well as the relatively weak H I 926 line, which shows the component structure.

At a lower velocity to the metal-poor cloud, we clearly detect H I, O VI and C III absorption at $v = +85$. Due to the obvious detection of O VI absorption, we label this absorber the “O VI cloud”. It is immediately apparent that the $N_{\text{H I}}$ is significantly lower in the O VI cloud than the metal-poor cloud, while the C III absorption strength is the same in both clouds. While O VI is lacking in the metal-poor cloud, it is clearly detected here. The HIRES spectra show no detection of Mg II in either cloud to sensitive limits (see Table 2).

We measured rest-frame equivalent widths of the absorption lines (W_r) by direct integration of the data, and the results are given in Table 2. To be conservative, we adopted the larger of the two Poisson error estimates in calculating equivalent width errors (see Section 2). We converted equivalent widths to column densities assuming the gas is optically thin (i.e. linear curve of growth) except where noted in the following section; saturated lines are given as lower limits.

For the O VI and unsaturated H I lines we generated apparent column density profiles (Savage & Sembach 1991). The apparent column density is defined as the observed normalized flux decrement in a given bin converted to a column density using the relation $N_a(v) = (3.767 \times 10^{14} \tau_a(v)) / (f \lambda)$ where $\tau_a(v) = \ln[I_c/I]$

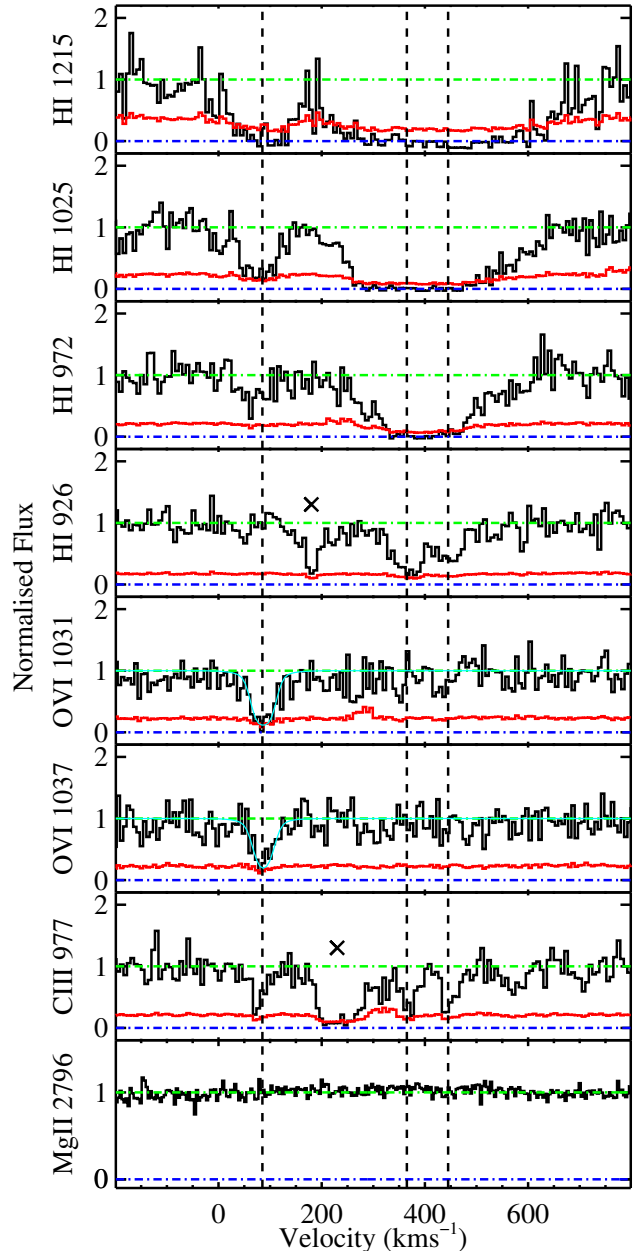


Figure 2. Velocity stack of detected lines in the O VI and metal-poor clouds. Strong absorption H I, O VI, and C III absorption can be seen at $v = 85 \text{ km s}^{-1}$, while the much strong H I absorption and weak C III absorption at $v = +365, 445 \text{ km s}^{-1}$ is due to the metal-poor cloud. Mg II is not detected in either the O VI or metal-poor cloud. Velocities are with respect to the systemic redshift of 227.19, $z_{\text{gal}} = 0.3529$. Small crosses mark absorption at other redshifts. Profile fits to the O VI absorption are shown overlaid in thin cyan lines. See below for details.

is the apparent optical depth, f is the oscillator strength of the transition, and λ is measured in \AA . Note that the continuum intensity I_c is unity for a continuum-normalized spectrum. The O VI and H I apparent column density profiles are shown in Fig 3.

3.2. Voigt Profile Fits

Since the metal lines come close to zero flux in several cases, we also performed Voigt profile fitting to check

Table 2
Measured column densities

Line	Velocity [km s^{-1}]	W_r [m\AA]	N [$\log \text{cm}^{-2}$]	Notes
Metal-poor cloud				
H I 1215	285	Inseparable
H I 1025	285	Inseparable
H I 972	285	97 ± 14	14.6 ± 0.1	
H I 949	285	81 ± 23	14.9 ± 0.1	
H I 937	285	72 ± 12	15.1 ± 0.1	
H I 1215	365	1765 ± 74	$> 14.5 \pm 0.1$	Saturated
H I 1025	365	1158 ± 35	$> 15.2 \pm 0.1$	Saturated
H I 972	365	586 ± 17	$> 15.4 \pm 0.1$	Saturated
H I 949	365	495 ± 28	$> 15.6 \pm 0.1$	Saturated
H I 937	365	214 ± 10	$> 15.5 \pm 0.1$	Saturated
H I 930	365	Blended
H I 926	365	169 ± 11	15.8 ± 0.1	
H I 923	365	Blended
H I 920	365	95 ± 13	15.9 ± 0.1	
H I 919	365	77 ± 12	15.9 ± 0.1	
C III 977	365	72 ± 10	13.0 ± 0.1	
C II 1036	365	± 12	< 13.0	Non-detection
O VI 1031	365	34 ± 16	< 13.2	Non-detection
Si III 1206	365	± 39	< 12.3	Non-detection
Mg II 2796	365	± 5	< 11.1	Non-detection
H I 1215	445	Inseparable
H I 1025	445	Inseparable
H I 972	445	Inseparable
H I 949	445	Inseparable
H I 937	445	187 ± 11	> 15.5	Saturated
H I 930	445	140 ± 11	15.6 ± 0.1	Blended?
H I 926	445	102 ± 12	15.6 ± 0.1	
H I 923	445	Blended
H I 920	445	87 ± 14	15.9 ± 0.1	
H I 919	445	39 ± 11	15.6 ± 0.1	
C III 977	445	80 ± 13	13.1 ± 0.1	
O VI 1031	445	36 ± 17	< 13.1	Non-detection
Si III 1206	445	± 33	> 12.2	Non-detection
O VI Cloud				
H I 1215	85	530 ± 47	> 14.0	Saturated
H I 1025	85	206 ± 18	14.4 ± 0.1	Saturated
H I 972	85	80 ± 16	14.5 ± 0.1	
H I 949	85	41 ± 28	14.6 ± 0.4	Non-detection
O VI 1031	85	150 ± 14	14.1 ± 0.1	
O VI 1037	85	107 ± 15	14.2 ± 0.1	
C III 977	85	71 ± 14	13.0 ± 0.1	
C II 1036	85	± 26	< 13.4	Non-detection
Si III 1206	85	± 42	< 12.4	Non-detection
Mg II 2796	85	± 4	< 11.0	Non-detection

Note. — Measured column densities for the metal-poor halo cloud at $v = +365 \text{ km s}^{-1}$, and the O VI cloud at $v = 85 \text{ km s}^{-1}$. Rest-frame equivalent widths are measured directly. Column densities are calculated assuming a linear curve-of-growth; lower limits are indicated for saturated lines, and 1σ upper limits for lines not detected. W_r is given as $\pm 1\sigma$ errors for non-detections. Cases of obvious blending with galactic absorption or other intervening systems are not reported.

for unresolved saturation. Fitting was performed on the O VI and C III lines in both clouds, and results are shown in Table 3.

Metal-poor Cloud

We fit the C III line in both strong components of the metal-poor cloud. The profile fits yield a higher column density (~ 0.4 dex) than is obtained in the optically thin case, but with correspondingly larger errors (~ 0.3 dex), such that the two measurements are in statistical agreement.

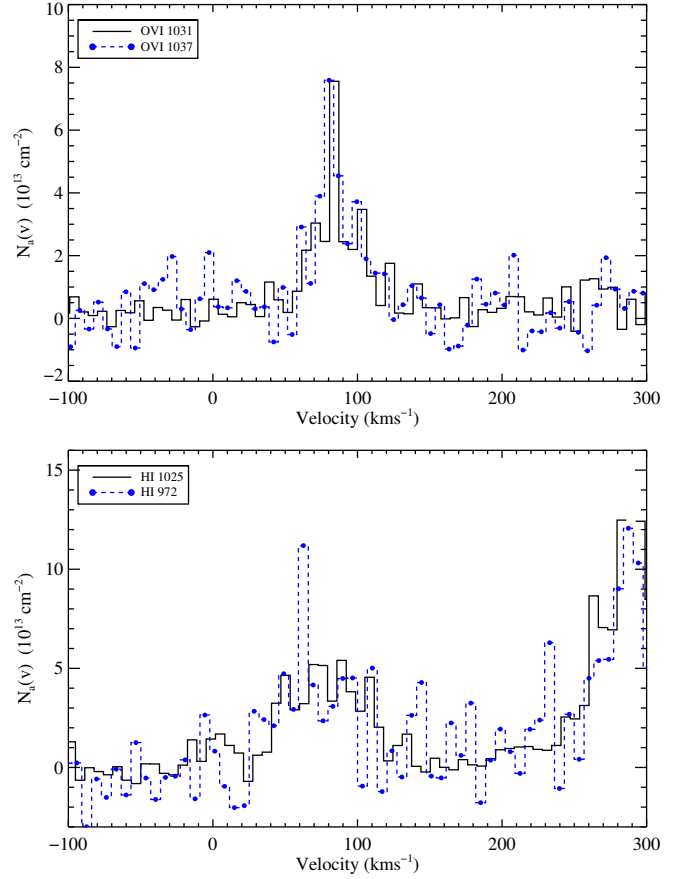


Figure 3. Comparison of apparent column density profiles. The top panel shows both members of the O VI doublet; the bottom panel shows the Ly β and Ly γ H I lines. Both sets of profiles are well matched. The O VI 1037 line shows an anomalous noise spike, which is apparent in the top blue (dashed) curve. In the bottom panel, the edge of the metal-poor cloud can be seen at $\sim 250 \text{ km s}^{-1}$.

O VI Cloud

The O VI apparent column density curves of the O VI cloud shown in Figure 3 show some evidence of asymmetry in the O VI profile, indicating that a two-component fit may be justified for the O VI. We performed fits using both a single and a double-component model, using two independent fitting codes, and taking into account the tabulated COS line-spread functions, but the S/N was not sufficient to distinguish between the two cases. This is reflected in the large parameter errors for the two component fit. The total column density is the same in with 1 or 2 components, and is ~ 0.4 dex higher than was obtained above by assuming the gas is optically thin. It is therefore likely that we are seeing a mild level of unresolved saturation. Since the profile fitting is more robust to saturation in the line core, it is a more reliable measure of the column density in the system. Moreover, the profile fits do not formally reach zero flux (see Figure 2), nor do the data show strong evidence of saturation, which leads us to believe that the unresolved saturation is mild, and we can confidently proceed by adopting the fitting results as our final O VI column densities.

The C III column density in the O VI cloud was also ~ 0.4 dex higher than predicted by the optically thin case, but the fitting errors were very large (0.6–0.7 dex).

Table 3
O VI Voigt profile fitting results

Line	v [km s^{-1}]	N [cm^{-2}]	b [km s^{-1}]
Metal Poor Cloud			
C III	369 ± 3	13.5 ± 0.2	13 ± 7
C III	447 ± 3	13.5 ± 0.3	12 ± 7
O VI Cloud—Single Component			
O VI	87 ± 2	14.6 ± 0.1	17 ± 3
C III	76 ± 3	13.5 ± 0.7	9 ± 8
O VI Cloud—Two Components			
O VI	84 ± 4	14.5 ± 0.2	14 ± 8
...	92 ± 12	14.2 ± 0.3	43 ± 23

Note. — Results of Voigt profile fits to metal lines.

Thus the C III column density in the O VI cloud is poorly constrained by the profile fitting, because the line is at best marginally resolved. This is shown clearly by the low doppler b -value, and correspondingly large errors in both N and b . This uncertainty in the C III column density is the dominant source of uncertainty in our analysis of the O VI cloud below. We also note that there is an 8 km s^{-1} offset in the centroids of the O VI and C III lines in the O VI cloud as a result of errors in the COS wavelength calibration.

3.3. Galaxy Star-Formation Rate and Metallicity

We determined the galaxy redshifts by fitting template spectra to the LRIS spectra. This template fitting is a modified version of the SDSS *zfind* code, which operates by fitting a linear combination of SDSS QSO eigenspectra to the galaxy spectrum (see Werk et al. 2011, for details). Galaxy 227_19, at $z_{\text{gal}} = 0.3529 \pm 0.0001$, is the only galaxy within $1'$ which is spectroscopically confirmed to be at the same redshift as the absorbers. In all cases, we use the redshift of the galaxy to set the systemic redshift, and measure velocity offsets from this redshift. The formal fitting error on the redshift is much less than the quoted redshift uncertainty, but systematic effects (e.g. in the wavelength calibration due to spectrograph flexure) limit the accuracy to $\sim 25 \text{ km s}^{-1}$, which we adopt as our redshift uncertainty. We recall, for comparison, that the COS resolution is $15 - 20 \text{ km s}^{-1}$. The galaxy spectrum shows a few, very weak emission lines and the S/N is not sufficient to detect any absorption. Despite the relative weakness of the emission lines, the redshift determination is confirmed by the detection of [O II], [O III] and H β . The spectrum of 227_19 is shown in Figure 4.

Since any star-formation rate (SFR) and metallicity indicators we derive depend sensitively on the measured line strength, care is needed when flux-calibrating the galaxy spectra. We attempt to ensure consistent flux calibration of both blue and red sides of the LRIS spectra. The seeing during the LRIS observations was not exceptional, so light losses from a $1''$ slit were corrected by comparing our spectra with SDSS photometry. We accomplish this absolute flux correction by convolving the LRIS spectra with SDSS *ugriz* filter response curves

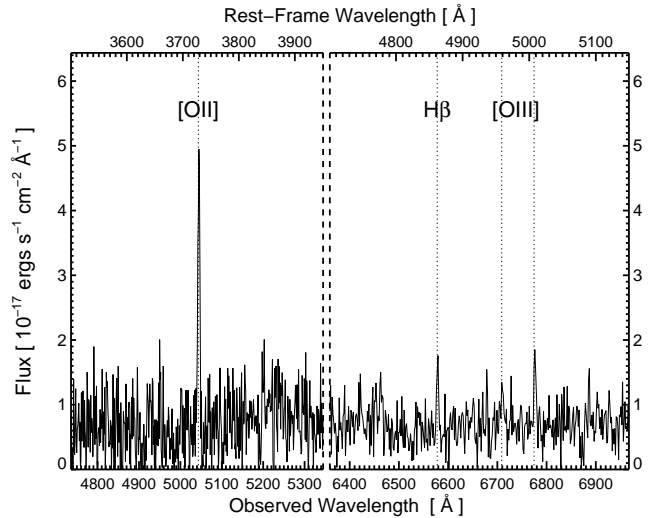


Figure 4. Keck/LRIS spectrum of galaxy 227_19. Weak emission lines of [O II] 3727, H β and [O III] 5007 can be seen, placing the galaxy at a redshift of $z_{\text{gal}} = 0.3529$.

(see Da Silva et al. 2011, for a description of the IDL code “spec2mag”), and comparing the observed spectral apparent magnitudes with the SDSS catalog apparent magnitudes (see Werk et al. 2011, for details). This process yields an independent multiplicative correction for both blue and red spectra. We derive flux correction factors of 2.2 for the blue side (0.88 mag in g -band) and 2.0 for the red side (0.75 mag in r -band). Note that this corresponds to slit losses of some 50 – 55%, and emphasizes the importance and difficulty of absolute flux calibration.

We took de-reddened magnitudes and colors for 227_19 from SDSS, and computed the distance modulus and absolute magnitude with the *kcorrect* software (Blanton & Roweis 2007) using the measured redshift, all of which are listed in Table 4. For comparison, we used the SDSS luminosity function parameters from Blanton et al. (2003). These parameters are strictly appropriate only for comparisons at $z = 0.1$ so for the calculation of the luminosity in Table 4 we correct to $z = 0.1$; in all other cases we correct to $z = 0$. We also used the H β emission line to derive a star-formation rate (SFR). H α is redshifted out of the LRIS wavelength range, but H β is detected. We estimate the SFR from the measured H β line flux, assuming a correction of $I(\text{H}\alpha) = 2.86 \times I(\text{H}\beta)$. This correction factor represents the intrinsic line ratio for case B recombination at 10^4 K and an electron density of 100 cm^{-3} (Hummer & Storey 1987). We use the relation $\text{SFR}(\text{H}\alpha) [\text{M}_{\odot} \text{ yr}^{-1}] = 5.45 \times 10^{-42} L(\text{H}\alpha) [\text{erg s}^{-1}]$ (Calzetti et al. 2010) to convert the measured luminosity $L(\text{H}\alpha) = 6.07 \times 10^{40} \text{ erg s}^{-1}$ into a SFR of $0.33 \pm 0.04 \text{ M}_{\odot} \text{ yr}^{-1}$. Note that we have only included statistical errors in the SFR. Other systematic errors in the calibration are likely to dominate the true error estimate. For example, we have no ability to determine the internal reddening correction, which may increase the derived star-formation rates by as much as a factor of 3, although the corrections are typically higher for higher SFRs (Rosa-González et al. 2002; Calzetti et al. 2007; Hunter et al. 2010).

We determined the oxygen metallicity of the star-

Table 4
Galaxy Properties

Galaxy ID	227_19
SDSS Name	J 094330.670+053118.1
z_{gal}	0.3529 ± 0.0001
m_u	22.5 ± 0.5
m_g	22.2 ± 0.1
m_r	21.0 ± 0.1
m_i	21.1 ± 0.1
m_z	20.9 ± 0.3
M_r	-20.4 ± 0.1
L^*	$0.4 L^*$
$g-r$	1.2
$u-r$	1.5
$L(\text{H}\beta)$	$2.12 \times 10^{40} \text{ erg s}^{-1}$
SFR ($\text{H}\alpha$)	$0.33 \pm 0.04 M_{\odot} \text{ yr}^{-1}$
$12 + \log(\text{O}/\text{H})$	8.48 ($0.6 Z_{\odot}$) Upper
$12 + \log(\text{O}/\text{H})$	8.26 ($0.4 Z_{\odot}$) Lower

Note. — Properties of galaxy at the approximate redshift of the absorption systems. The Galaxy ID is a polar co-ordinate system based on the position angle and radius (in arcsec), centered on the QSO position. Magnitudes are SDSS magnitudes corrected for MW dust extinction.

forming regions in 227_19 using the R23 metallicity indicator (Pagel et al. 1979), calibrated by McGaugh (1991). R23 is defined as $([\text{O II}] + [\text{O III}])/\text{H}\beta$ and is easily measured. The R23 indicator has a well-known degeneracy and turnover at $\sim 0.3 Z_{\odot}$ and large systematic errors (on the order of 0.25 dex) due to age effects and stellar distributions (Ercolano et al. 2007). Despite these drawbacks, it provides the only available estimate of the galaxy metallicity from the spectrum of 227_19. Unlike the SFR estimate, the R23 indicator is not as susceptible to internal reddening because the emission lines are close in wavelength. Further, since 227_19 lies close to the turnover in the R23 indicator (see, for example, McGaugh 1991, Figure 12), even a significant amount of internal reddening will have only a minor effect on the metallicity, and this will be much less than the intrinsic systematic error.

We corrected the emission lines for foreground reddening using a standard Galactic reddening law with $R_v = 3.1$ with $E(B-V) = 0.04$ (Schlegel et al. 1998). Since our spectra do not show $[\text{N II}]$ emission lines, we are unable to break the degeneracy in the R23 indicator, so we report both upper and lower branch metallicities, obtaining the range $0.4 - 0.6 Z_{\odot}$. In calculating the metallicity, we use the most recent solar Oxygen abundance of $12 + \log(N_{\text{O}}/N_{\text{H}}) = 8.69$ from Asplund et al. (2009). Table 4 lists a summary of all our measured and derived galaxy properties.

4. DISCUSSION

4.1. Galaxy-Absorber Connection

Metal-poor cloud at $v = +365 \text{ km s}^{-1}$

At a redshift of $z_{\text{gal}} = 0.3529$, the $19''$ angular distance between galaxy 227_19 corresponds to $\sim 95 \text{ kpc}$. The velocity separation between the two components of the metal-poor cloud and the galaxy is substantial ($\Delta v = +365, +445 \text{ km s}^{-1}$). By comparison, the Milky Way halo contains clouds moving at radial velocities of

up to $\sim 450 \text{ km s}^{-1}$ (Wakker & van Woerden 1991; Putman et al. 2002; Peek et al. 2007), so it is not unreasonable that this cloud is associated with 227_19. By analogy with the MW, we may consider the main absorption low-metallicity infalling material. For this analogy to hold, we must consider what both the observed SFR and the cloud metallicity can tell us. Let us consider these two issues in turn.

If we consider a scenario in which this cloud is part of an outflow from the main galaxy, we must reconcile both the low SFR in the host galaxy 227_19, and consider the metallicities. The travel time to an assumed distance $d > 95 \text{ kpc}$ at the observed velocity difference 365 km s^{-1} is some $\sim 250 \text{ Myr}$. Star-formation induced outflows can be driven by the correlated supernovae of early type stars in OB associations (Mac Low & McCray 1988). Since those stars have typical lifetimes of only $\lesssim 10 \text{ Myr}$ (Meynet et al. 1994), much shorter than the minimum travel time to the observed distance of 95 kpc, the current observed SFR does not provide a constraint on the gas origin.

Next let us consider the metallicity. The observed H I and C III column densities in both strong components are the same (to within 0.1–0.2 dex), with $\log N_{\text{H I}} \sim 16$ and $\log N_{\text{C III}} \sim 13.5$. At these H I column densities, we should expect to see appreciable absorption columns from metal lines in gas enriched to greater than a few tenths solar. Indeed, we see similar strength of absorption in C III in the O VI cloud as the metal-poor cloud, but the O VI cloud has more than $25\times$ lower $N_{\text{H I}}$. This points to the possibility that the cloud is metal-poor, but is not conclusive, since ionization corrections may be significant.

To quantify this assertion of low metallicity, we attempted simple ionization modeling. The relative lack of metal lines makes detailed modeling impossible, but the C III detection, as well as the C II, Mg II and O VI upper limits gives us some direction. We examined grids of *Cloudy* photoionization models (version 08.00; Ferland et al. 1998), varying both the metallicity and the dimensionless ionization parameter $\log U$ (the ratio of the density of hydrogen ionizing photons to total hydrogen density), integrating to a fixed $\log N_{\text{H I}} = 16.0$. We used the updated ‘‘HM05’’ UV background spectrum, which is the average UV background produced by AGN and starburst galaxies (Haardt & Madau 1996); we did not include a contribution from nearby star-formation. Tumlinson et al. (2011) give a relation to derive the contribution of star-forming regions to the UV background, as a function of escape fraction, distance and SFR. At a distance of $d > 95 \text{ kpc}$ and $\text{SFR} = 0.33 \pm 0.04 \text{ Myr}$, star formation contributes to the ionization field at the level of a few percent for reasonable values of the escape fraction of ionizing photons (i.e. $f_{\text{esc}} < 0.04$; Putman et al. 2003a; Chen et al. 2007). Note also that photoionization of O V to O VI requires photons with energies of 114 eV or greater, which cannot be supplied by star-formation.

Figure 5 shows contours of the predicted column densities in metallicity- $\log U$ space for these cloudy models. As can be seen, the Mg II and C II non-detections provide tight constraints on the metallicity, although this restriction relaxes at high ionization parameter (low density). The O VI non-detection limits the allowed region

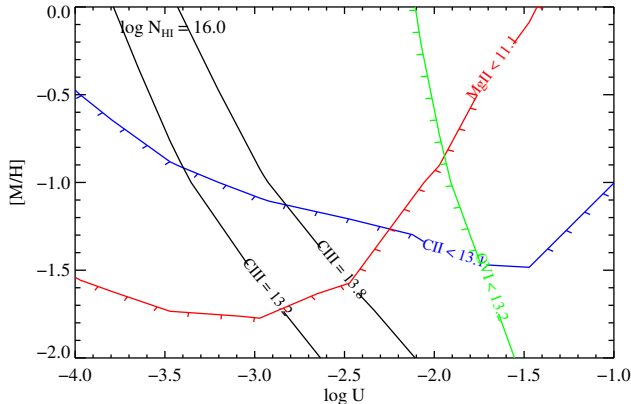


Figure 5. Column contours predictions from photoionization model of the metal-poor cloud. Limits are given based on the measurements from Table 2. Small tick marks on the contours indicate the allowed region of parameter space for upper limits.

of parameter space to $\log U < -1.5$, but the combined detection of C III and non-detection of Mg II is the most restrictive. These combine to limit the metallicity of the cloud to $[M/H] < -1.5$. At this point, it is worth emphasizing the value of the follow-up HIRES optical spectrum. Without it, the metallicity would be significantly less constrained, and our interpretation much less certain.

The combination of the high velocity relative to the galaxy, the low metallicity, and the large distance from the galaxy leads us to the conclusion that the halo cloud at $v = +365 - 445 \text{ km s}^{-1}$ is an accreting, metal-poor gas cloud, providing fuel for future star formation in galaxy 227_19.

O VI cloud at $v = 85 \text{ km s}^{-1}$

The velocity separation between the O VI cloud and galaxy is $\Delta v = 85 \text{ km s}^{-1}$, which is typically close enough to consider the gas to exist in the galaxy halo. It is interesting to note that a cloud with such a low velocity in the MW halo may not even be classified as a halo cloud, given its low velocity separation from the galaxy. Rather, the O VI cloud would likely be considered part of the $\sim 3 \text{ kpc}$ high, ionized gas surrounding the thick disk (c.f. Savage et al. 2003), as opposed to a distant halo cloud. The detection of O VI at a distance $d \geq 95 \text{ kpc}$ from the disk may have implications for the interpretation of the MW O VI halo clouds.

To interpret the O VI cloud, we considered the feasibility of several scenarios to explain physical conditions of the cloud. In doing so, we adopt the single component metal-line column densities from the Voigt profile fitting in the previous section (Table 3). The principle source of error, which propagates to our derived physical quantities, is the large permitted range of C III column density.

A pure collisional ionization equilibrium (CIE) model can be quickly excluded by examination of the absorption line widths and column density. O VI traces collisionally ionized gas in the range $\log T = 5.2 - 6.5$, peaking at $\log T = 5.5$ (Sutherland & Dopita 1993; Gnat & Sternberg 2007). O VI and C III may coexist at the low end of this range, but the $N_{\text{O VI}} / N_{\text{C III}}$ ratio is a very steep

function of temperature; the measured range in the column density ratio $N_{\text{O VI}} / N_{\text{C III}} = 0.6 - 1.7$ allows temperatures only in the narrow range $\log T = 5.25 - 5.3$. At this temperature, the implied thermal doppler line-width for H I is $b_{\text{therm}} = \sqrt{2kT/m} = 57 \text{ km s}^{-1}$, or a full-width at half-maximum width of 94 km s^{-1} . This line width is clearly excluded by a visual inspection of the data; a Voigt profile fit (accounting for the COS line-spread function) yields $b_{\text{H I}} \simeq 32 \text{ km s}^{-1}$, confirming that a pure collisional ionization equilibrium model is ruled out.

The detection of both C III and O VI, and the limits on C II and Mg II column densities give us some handle on a simple photoionization scenario. Simple plane-parallel *Cloudy* photoionization models with the canonical HM05 spectrum can reproduce the observed metal line column densities and line ratios. The ratio of $N_{\text{O VI}}$ to $N_{\text{C III}}$ fixes the range of allowed ionization parameter (and hence density), since the column density ratio is independent of metallicity for a fixed abundance pattern, and the UV background is also fixed. The allowed metallicity range can then be obtained using the permitted density ranges, and varying the metallicity until the observed column densities are obtained.

The observed conditions are reproduced for a model with $\log U = -1.1 - -0.4$ and metallicity in the range $[M/H] = -0.3 - -1.1$ for a solar abundance pattern. Given the input HM05 spectrum is fixed at all points (and hence the number of ionizing photons is also fixed), this $\log U$ range corresponds to a density range $\log n_{\text{H}} = -4.4 - -4.9$. However, this assumes both the shape and normalization of the UV spectrum is known and equal to the HM05 spectrum (which is simply the *average* spectrum); the true normalization and shape are still quite uncertain (c.f. Scott et al. 2002; Shull et al. 1999). We have no ability to determine the true shape or normalization of the radiation field (i.e. our data do not show any density diagnostics), so we can only proceed using the canonical UV background field; nevertheless, this should be kept in mind. A plot of the predicted metal line column densities as a function of $\log U$ and n_{H} is shown in Figure 6. To construct this plot, we took the metallicity to be $[M/H] = -0.7$, in the middle of the allowed range. The vertical dashed lines mark the range of density/ionization parameter permitted by the O VI to C III column density ratio.

At these densities, the fraction of hydrogen in neutral form is extremely low ($10^{-4.5} - -5.1$). To obtain the observed neutral hydrogen column density of $\log N_{\text{H I}} = 14.6$ at this ionization fraction and physical density would require a cloud with a length scale $L \sim 0.1 - 1.2 \text{ Mpc}$. A cloud with this physical size is unlikely to be a distinct cloud in a galaxy halo, but the length scale is consistent with absorption arising in a large-scale filamentary structure (i.e. the Ly α forest) or a galaxy group (see, for example Schaye 2001). Intragroup gas has separately been suggested as a possible origin for highly ionized species such as O VI (Mulchaey et al. 1996) and a few examples have been observed, both in the Local Group and the low- z IGM (Tripp & Savage 2000; Nicastro et al. 2003).

In order to assess a possible group origin, we examined galaxies in the field near 227_19 using available SDSS

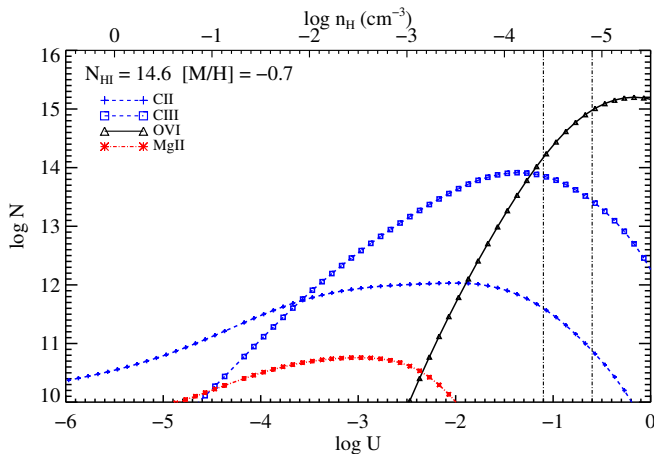


Figure 6. Column density predictions from photoionization model of the O VI cloud. The model assumed a plane-parallel geometry, illuminated by the HM05 UV background spectrum, integrated to $N_{\text{HI}} = 10^{14.6}$ with $[\text{M}/\text{H}] = -0.7$. Vertical dashed lines show the region allowed by the observed O VI to C III column density ratio.

data. We took the photometric redshift estimates⁸ for galaxies in the surrounding region as given by Cunha et al. (2009). The closest potential group candidate is a set of three galaxies ~ 1 Mpc to the NNW: all are brighter than $0.4L^*$ if they are at the redshift of the absorber, and have photometric redshift probability distributions $p(z)$ broadly consistent with $z = 0.35$. The $0.4L^*$ level is typically used in structure-finding algorithms, exploiting the red sequence of galaxies in large virialized structures such as groups and clusters (see, e.g. Koester et al. 2007); the fact that 227_19 is also $0.4L^*$ is coincidental.

With such a small number of galaxies, the radius of such a system would be only $r_{200} \sim 0.4$ Mpc (Hansen et al. 2009) and would not encompass 227_19. There are a number of galaxies in the vicinity of 227_19 which have photometric redshifts broadly consistent with $z = 0.35$, but all are fainter than $0.4L^*$. These galaxies lie primarily to the S. We thus conclude that 227_19 probably does not exist in a galaxy group, and that the O VI does not therefore arise from the group environment. This conclusion is also consistent with the above finding that CIE models do not adequately describe the data. We are thus left with the possibility that the O VI arises in a filament. Spectroscopic confirmation of these faint galaxies is required to further investigate the filamentary structure hypothesis.

To check the physical consistency of the filament scenario, we compared the measured properties of the O VI cloud to the IGM equation of state predictions of Ricotti et al. (2000). At a density $n_{\text{H}} = -4.4$ to -4.9 , the cosmic overdensity is $\delta \simeq 12$ – 37 . Using this overdensity and the effective IGM equation of state (EOS), $T = T_0(1 + \delta)^{\gamma-1}$ from Ricotti et al. (2000), we can derive the implied thermal Doppler parameter for H I. We interpolate between redshifts in their Table 6 to obtain EOS parameters $T_0 = 7.1 \times 10^3$ K and $\gamma - 1 = 0.75$ for $z = 0.4$. This resulting EOS then predicts temperatures in the range

⁸ Photometric redshifts are especially challenging to accurately determine at $z = 0.35$, due to the 4000 \AA break moving from the g to r bands, and the $p(z)$ distributions of these systems are correspondingly broad.

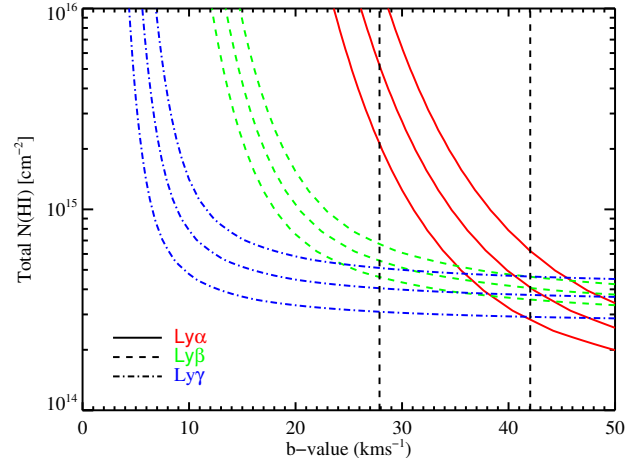


Figure 7. Curve of growth for the H I lines in the O VI cloud. The curves show the measured value and $\pm 1\sigma$ error bars. The vertical dashed line shows the prediction from the IGM equation of state. See text for details.

$\log T = 4.6$ – 5.0 K and $b_t = (2kT/m)^{0.5} = 28$ – 43 km s^{-1} .

To compare to this predicted Doppler parameter with the measurements, we performed a curve of growth analysis on the 3 strongest Lyman series lines in the O VI cloud. The results are shown in Figure 7. The vertical dashed lines show the Doppler parameter predicted by the IGM EOS. The curve of growth shows a broad region of allowed Doppler parameters, which are consistent with the theory predictions. We conclude that the absorber has a density, ionization state, cloud size, and line broadening consistent with a filament of the large scale structure. While we observe that some galaxies in the region around 227_19 have photometric redshift estimates consistent with $z = 0.35$, a more detailed spectroscopic survey of the large-scale galaxy distribution around 227_19 is necessary to confirm this suggestion. In addition, the principle source of error in constraining the physical conditions of the O VI cloud is the large range of column densities allowed by the fits to the C III line. A higher resolution and/or higher signal-to-noise spectrum would allow us to be more precise about the physical conditions, but is unlikely to alter the broad conclusions.

5. CONCLUSION

We have presented the observations of two gaseous structures near or in the halo of a galaxy at $z = 0.35$. Absorption lines due to an enriched gas filament and in-falling metal-poor cloud are detected with small velocity offsets from the systemic galaxy redshift. The metal-poor cloud has strong H I absorption ($\sim 10^{16} \text{ cm}^{-2}$) and weak metal lines, with only weak lines of C III. A sensitive non-detection of Mg II in the optical high resolution spectrum, combined with the observed C III line strengths, indicates this cloud is metal-poor ($[\text{M}/\text{H}] < -1.5$).

The other absorber contains strong O VI absorption, and is consistent with arising in cool photoionized gas at modest overdensities ($\log n_{\text{H}} = -4.4$ – -4.9 ; $\delta \simeq 12$ – 37). At these densities, the implied length scale for the H I is ~ 0.1 – 1.2 Mpc leading to the suggestion that the gas arises in a group or filament. At an impact parameter $\rho = 95 \text{ kpc}$ and velocity separation $\Delta v = 85 \text{ km s}^{-1}$, a casual inspection would reasonably associate the O VI

absorption with the galaxy halo; this example serves as a cautionary tale against such association. Inspection of photometric redshifts for nearby galaxies reveals several faint galaxies consistent with being at $z = 0.35$, but there are no bright galaxies ($L > 0.4L^*$ at $z = 0.35$) nearby, which argues against the gas arising in an intragroup environment, and hence the gas most likely exists in a filament. Spectroscopic followup of galaxies in the field is required to confirm this conclusion.

In our analysis of both clouds, we detected a mild level of unresolved saturation. This is likely to occur in many low signal-to-noise data ($S/N < 10$), and is likely to be especially problematic for metal lines, which are intrinsically narrow.

When complete, our survey will provide some 80 QSO sightlines similar to those presented here, that are selected to pass through the halos of galaxies at a range of luminosities, colors and impact parameters. Observations such as these are required to unravel the connection between gas and galaxies, an increasingly important part of the galaxy evolution puzzle. They may also provide context for the interpretation of observations of the Milky Way halo.

C. T. thanks Sarah Hansen for helpful discussions on the selection of galaxy groups from photometric redshift data. We thank Derck Massa for providing early copies of the COS flat field corrections, and Edward Jenkins for his careful processing of the flats. Support for program GO 11598 was provided by NASA through a grant from the Space Telescope Science Institute, which is operated by the Association of Universities for Research in Astronomy, Inc., under NASA contract NAS 5-26555. J. X. P. and J. W. acknowledge partial support from NSF CAREER grant AST-0548180. Some of the data presented herein were obtained at the W.M. Keck Observatory, which is operated as a scientific partnership among the California Institute of Technology, the University of California and the National Aeronautics and Space Administration. The Observatory was made possible by the generous financial support of the W.M. Keck Foundation. The authors wish to recognize and acknowledge the very significant cultural role and reverence that the summit of Mauna Kea has always had within the indigenous Hawaiian community. We are most fortunate to have the opportunity to conduct observations from this mountain.

HST(COS); Keck(LRIS); Keck(HIRES)

REFERENCES

- Asplund, M., Grevesse, N., Sauval, A. J., & Scott, P. 2009, *ARA&A*, 47, 481
- Barnes, D. G., et al. 2001, *MNRAS*, 322, 486
- Ben Bekhti, N., Richter, P., Westmeier, T., & Murphy, M. T. 2008, *A&A*, 487, 583
- Birnboim, Y., & Dekel, A. 2003, *MNRAS*, 345, 349
- Blanton, M. R., & Roweis, S. 2007, *AJ*, 133, 734
- Blanton, M. R., et al. 2003, *ApJ*, 592, 819
- Bregman, J. N., & Lloyd-Davies, E. J. 2007, *ApJ*, 669, 990
- Calzetti, D., et al. 2007, *ApJ*, 666, 870
- . 2010, *ApJ*, 714, 1256
- Chen, H., & Mulchaey, J. S. 2009, *ApJ*, 701, 1219
- Chen, H., Prochaska, J. X., & Gnedin, N. Y. 2007, *ApJ*, 667, L125
- Collins, J. A., Shull, J. M., & Giroux, M. L. 2009, *ApJ*, 705, 962
- Cunha, C. E., Lima, M., Oyaizu, H., Frieman, J., & Lin, H. 2009, *MNRAS*, 396, 2379
- Da Silva, R., Prochaska, J. X., Rosario, D., Tumlinson, J., & Tripp, T. M. 2011, *ApJ*, submitted
- Danforth, C. W., Keeney, B. A., Stocke, J. T., Shull, J. M., & Yao, Y. 2010, *ApJ*, 720, 976
- Danforth, C. W., & Shull, J. M. 2008, *ApJ*, 679, 194
- Ercolano, B., Bastian, N., & Stasińska, G. 2007, *MNRAS*, 379, 945
- Ferland, G. J., Korista, K. T., Verner, D. A., Ferguson, J. W., Kingdon, J. B., & Verner, E. M. 1998, *PASP*, 110, 761
- Gehrels, N. 1986, *ApJ*, 303, 336
- Gnat, O., & Sternberg, A. 2007, *ApJS*, 168, 213
- Green, J. C., Wilkinson, E., & Morse, J. A. 2003, in *Society of Photo-Optical Instrumentation Engineers (SPIE) Conference Series*, Vol. 4854, Society of Photo-Optical Instrumentation Engineers (SPIE) Conference Series, ed. J. C. Blades & O. H. W. Siegmund, 72–80
- Haardt, F., & Madau, P. 1996, *ApJ*, 461, 20
- Hansen, S. M., Sheldon, E. S., Wechsler, R. H., & Koester, B. P. 2009, *ApJ*, 699, 1333
- Heitsch, F., & Putman, M. E. 2009, *ApJ*, 698, 1485
- Hummer, D. G., & Storey, P. J. 1987, *MNRAS*, 224, 801
- Hunter, D. A., Elmegreen, B. G., & Ludka, B. C. 2010, *AJ*, 139, 447
- Kalberla, P. M. W., Burton, W. B., Hartmann, D., Arnal, E. M., Bajaja, E., Morras, R., & Pöppel, W. G. L. 2005, *A&A*, 440, 775
- Kauffmann, G., et al. 2003, *MNRAS*, 341, 54
- Kereš, D., Katz, N., Fardal, M., Davé, R., & Weinberg, D. H. 2009, *MNRAS*, 395, 160
- Koester, B. P., et al. 2007, *ApJ*, 660, 221
- Lehner, N., & Howk, J. C. 2010, *ApJ*, 709, L138
- Lehner, N., Prochaska, J. X., Kobulnicky, H. A., Cooksey, K. L., Howk, J. C., Williger, G. M., & Cales, S. L. 2009, *ApJ*, 694, 734
- Münch, G., & Zirin, H. 1961, *ApJ*, 133, 11
- Mac Low, M., & McCray, R. 1988, *ApJ*, 324, 776
- McGaugh, S. S. 1991, *ApJ*, 380, 140
- Meiring, J. D., et al. 2011, *ApJ*, in press
- Meynet, G., Maeder, A., Schaller, G., Schaerer, D., & Charbonnel, C. 1994, *A&AS*, 103, 97
- Mulchaey, J. S., Mushotzky, R. F., Burstein, D., & Davis, D. S. 1996, *ApJ*, 456, L5
- Muller, C. A., Oort, J. H., & Raimond, E. 1963, *Comptes Rendus de l'Académie des Sciences Paris*, 257, 1661
- Nicastro, F., et al. 2003, *Nature*, 421, 719
- Oke, J. B., et al. 1995, *PASP*, 107, 375
- Oppenheimer, B. D., & Davé, R. 2009, *MNRAS*, 395, 1875
- Pagel, B. E. J., Edmunds, M. G., Blackwell, D. E., Chun, M. S., & Smith, G. 1979, *MNRAS*, 189, 95
- Peek, J. E. G., Heiles, C., Putman, M. E., & Douglas, K. 2009, *ApJ*, 692, 827
- Peek, J. E. G., Putman, M. E., McKee, C. F., Heiles, C., & Stanimirović, S. 2007, *ApJ*, 656, 907
- Prochaska, J. X., Weiner, B., Chen, H. W., Mulchaey, J., & Cooksey, K. 2011, *ApJ*, submitted
- Prochaska, J. X., Weiner, B. J., Chen, H.-W., & Mulchaey, J. S. 2006, *ApJ*, 643, 680
- Putman, M. E., Bland-Hawthorn, J., Veilleux, S., Gibson, B. K., Freeman, K. C., & Maloney, P. R. 2003a, *ApJ*, 597, 948
- Putman, M. E., Staveley-Smith, L., Freeman, K. C., Gibson, B. K., & Barnes, D. G. 2003b, *ApJ*, 586, 170
- Putman, M. E., et al. 2002, *AJ*, 123, 873
- Quilis, V., & Moore, B. 2001, *ApJ*, 555, L95
- Richter, P., Westmeier, T., & Brüns, C. 2005, *A&A*, 442, L49
- Ricotti, M., Gnedin, N. Y., & Shull, J. M. 2000, *ApJ*, 534, 41
- Rosa-González, D., Terlevich, E., & Terlevich, R. 2002, *MNRAS*, 332, 283
- Savage, B. D., Narayanan, A., Lehner, N., & Wakker, B. P. 2011, *ArXiv e-prints*
- Savage, B. D., & Sembach, K. R. 1991, *ApJ*, 379, 245
- Savage, B. D., Tripp, T. M., & Lu, L. 1998, *AJ*, 115, 436
- Savage, B. D., et al. 2003, *ApJS*, 146, 125
- . 2010, *ApJ*, 719, 1526
- Schaye, J. 2001, *ApJ*, 559, 507
- Schlegel, D. J., Finkbeiner, D. P., & Davis, M. 1998, *ApJ*, 500, 525

- Scott, J., Bechtold, J., Morita, M., Dobrzycki, A., & Kulkarni, V. P. 2002, *ApJ*, 571, 665
- Sembach, K. R., et al. 2003, *ApJS*, 146, 165
- Shull, J. M., Roberts, D., Giroux, M. L., Penton, S. V., & Fardal, M. A. 1999, *AJ*, 118, 1450
- Spitzer, L. J. 1956, *ApJ*, 124, 20
- Stoche, J. T., Penton, S. V., Danforth, C. W., Shull, J. M., Tumlinson, J., & McLin, K. M. 2006, *ApJ*, 641, 217
- Strateva, I., et al. 2001, *AJ*, 122, 1861
- Sutherland, R. S., & Dopita, M. A. 1993, *ApJS*, 88, 253
- Thom, C., & Chen, H.-W. 2008a, *ApJ*, 683, 22
- . 2008b, *ApJS*, 179, 37
- Thom, C., Peek, J. E. G., Putman, M. E., Heiles, C., Peek, K. M. G., & Wilhelm, R. 2008, *ApJ*, 684, 364
- Thom, C., Putman, M. E., Gibson, B. K., Christlieb, N., Flynn, C., Beers, T. C., Wilhelm, R., & Lee, Y. S. 2006, *ApJL*, 638, L97
- Tremonti, C. A., et al. 2004, *ApJ*, 613, 898
- Tripp, T. M., Aracil, B., Bowen, D. V., & Jenkins, E. B. 2006, *ApJ*, 643, L77
- Tripp, T. M., Giroux, M. L., Stoche, J. T., Tumlinson, J., & Oegerle, W. R. 2001, *ApJ*, 563, 724
- Tripp, T. M., & Savage, B. D. 2000, *ApJ*, 542, 42
- Tripp, T. M., Sembach, K. R., Bowen, D. V., Savage, B. D., Jenkins, E. B., Lehner, N., & Richter, P. 2008, *ApJS*, 177, 39
- Tripp, T. M., & Song, L. 2011, *ArXiv e-prints*
- Tripp, T. M., et al. 2003, *AJ*, 125, 3122
- Tumlinson, J., Werk, J. E., Thom, C., Meiring, J., Prochaska, J. X., Tripp, T. M., Okrochkov, M., & Sembach, K. R. 2011, *ApJ*, submitted
- van Woerden, H., Schwarz, U. J., Peletier, R. F., Wakker, B. P., & Kalberla, P. M. W. 1999, *Nature*, 400, 138
- Vogt, S. S., et al. 1994, in Presented at the Society of Photo-Optical Instrumentation Engineers (SPIE) Conference, Vol. 2198, Proc. SPIE Instrumentation in Astronomy VIII, David L. Crawford; Eric R. Craine; Eds., Volume 2198, p. 362, ed. D. L. Crawford & E. R. Craine, 362–+
- Wakker, B. P., & van Woerden, H. 1991, *A&A*, 250, 509
- . 1997, *ARA&A*, 35, 217
- Wakker, B. P., York, D. G., Wilhelm, R., Barentine, J. C., Richter, P., Beers, T. C., Ivezić, Ž., & Howk, J. 2007, *ApJ* submitted (arXiv:0709.1926)
- Wang, Q. D., et al. 2005, *ApJ*, 635, 386
- Werk, J. E., Prochaska, J. X., Meiring, J., Thom, C., Tripp, T. M., & Tumlinson, J. 2011, *ApJ*, in prep
- Westmeier, T., Brüns, C., & Kerp, J. 2005, *A&A*, 432, 937
- White, S. D. M., & Rees, M. J. 1978, *MNRAS*, 183, 341
- Yao, Y., Shull, J. M., Danforth, C. W., Keeney, B. A., & Stoche, J. T. 2011, *ArXiv e-prints*
- York, D. G., et al. 2000, *AJ*, 120, 1579